Chemical Engineering Journal 341 (2018) 83–92

Contents lists available at ScienceDirect

Chemical Engineering Journal

journal homepage: www.elsevier.com/locate/cej

Enhanced photocatalytic performance of Ag@TiO_2 for the gaseous acetaldehyde photodegradation under fluorescent lamp

Qinglong Zeng[a,b], Xiaofeng Xie[a,*], Xiao Wang[a], Yan Wang[a], Guanhong Lu[a], David Y.H. Pui[c], Jing Sun[a]

[a] Shanghai Institute of Ceramics, Chinese Academy of Sciences, Shanghai 200050, China
[b] University of Chinese Academy of Sciences, 19 Yuquan Road, Beijing 100049, China
[c] College of Science and Engineering, University of Minnesota, Minneapolis, MN 55455, USA

HIGHLIGHTS

- The Ag@TiO_2 core-shell structure is beneficial to more light absorption and efficient charge separation.
- The adsorptive property of acetaldehyde could reflect the effective reactive sites more straight in comparison to S_{BET}.
- The roles of reactive radicals were investigated through combining ESR tests and scavenger experiments together.
- $^{\cdot}O_2^-$ played the predominant role in the photocatalytic process of acetaldehyde.

GRAPHICAL ABSTRACT

The outstanding performance of Ag nanowires@TiO_2 composite and the thoroughly understanding of acetaldehyde photodegradation mechanism would cast light on the purposively design and optimization of TiO_2-based catalysts.

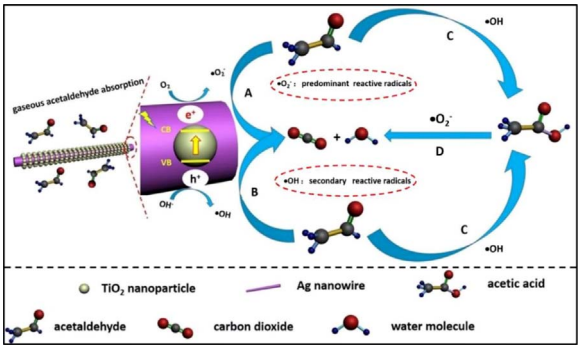

ARTICLE INFO

Keywords:
Surface plasmon resonance
Gaseous photocatalysis
Ag@TiO_2 core-shell heterostructure
Reactive radicals
Photocatalytic mechanism

ABSTRACT

The ever increasing problem of air pollution has provoked the research and development of highly-efficient photocatalysts. Herein, Ag nanowires@TiO_2 composite photocatalyst with improved photocatalytic performance was fabricated by a facile one-step solvothermal procedure. The formation of one-dimensional Ag nanowires@TiO_2 core-shell nanostructures could not only broaden the light-absorbing range of TiO_2 catalysts through the surface plasmon resonance effect of Ag nanowires, but also enable the effective separation of photoinduced electron-hole pairs. Under the irradiation of a 260 W fluorescent lamp, the composite with 0.5 wt % Ag nanowires exhibited the highest photocatalytic activity in short contact time (4.8 min), and the corresponding gaseous acetaldehyde removal ratio was 72%, which was much higher than that of bare TiO_2 (37%). The photocatalyst also showed ultrastable activity in the 15 weeks usage, which ensured their practical applications in the air purification field. An in-depth mechanism of the photodecomposition of acetaldehyde was proposed on the basis of the electron spin resonance (ESR) tests and the scavenger experiments. $^{\cdot}O_2^-$ reactive radicals was found to play a predominant role in the oxidation and decomposition of acetaldehyde. The outstanding performance of the composite materials and the thoroughly understanding of the reaction mechanism would cast light on the purposively design and optimization of TiO_2-based catalysts.

* Corresponding author.
E-mail address: xxfshcn@163.com (X. Xie).

https://doi.org/10.1016/j.cej.2018.02.015
Received 4 November 2017; Received in revised form 4 February 2018; Accepted 5 February 2018
Available online 06 February 2018
1385-8947/

1. Introduction

Nowadays, with the rapid industrial development and the huge consumption of fossil fuels, diverse gaseous pollutants have been released into our living environment, which has resulted in serious environmental problems, including acid rain, photochemical smog and haze [1,2]. Many efforts have been made to solve this troublesome issue. Among all the possible solutions, photocatalysis is an ambient temperature process which can make use of solar energy to photodecompose various organic contaminants without secondary pollution. However, most of the research works today concentrate on the photodecomposition of liquid pollutants such as Methyl Orange (MO) and Rhodamine B (RhB) [3]. Due to the intrinsic differences between the photodecomposition of liquid pollutants and gaseous pollutants, traditional photocatalysts suitable for liquid pollutants cannot be applied to the decomposition of gaseous pollutants directly [4]. The decomposition of pollutants relies on the adsorption of pollutants on the surface of photocatalysts. Unlike liquid pollutants, the concentration of gaseous pollutants is relatively low. The fast and disordered movement of gas molecules further lowered the residue time of gaseous pollutants. The lower concentration of pollutants and the shorter residue time proposed a higher requirement for the photocatalytic capacity and adsorption ability of photocatalysts.

TiO_2 has long been regarded as an ideal photocatalyst to deal with environmental concerns, owing to its non-toxicity, environmentally benign nature, low-cost, abundance, chemical and thermal stability [3–8]. Despite all those advantages, TiO_2 is still being criticized for its poor light-harvesting capacity and the rapid recombination rate of photoinduced electron-hole pairs, which has limited the photocatalyst capacity of TiO_2-based photocatalysts and its applications in the photodecomposition of gaseous pollutants. Only 4% solar energy can be utilized by TiO_2 due to its wide band gap (3.2 eV) [9]. In order to make full use of the abundant solar energy resource, the development of TiO_2 photocatalysts with enhanced light-harvesting capacity is indispensable [10,11]. On the other hand, the rapid recombination of electron–hole pairs, which is harmful to the photocatalytic performance of catalysts, should be suppressed effectively [12–14]. Reviews [15–18] have revealed that the formation of TiO_2 heterostructures often brings some attractive benefits for the photocatalysts. Works have been done to optimize the performance of TiO_2-based photocatalysts. Li et al. [19] and Lu et al. [20] enhanced the light-harvesting capacity of TiO_2 by coupling it with C_3N_4. The utilization of the surface plasmon resonance effect (SPR) of noble metals is an effective way in the optimization of TiO_2 catalysts [21–24]. Under the illumination of light with certain wavelength, the free electrons of the noble metals such as Au, Ag or Pt nanoparticles would couple with the incident light at a resonant frequency, which leads to a localized electronic field around the metal nanoparticles and results in the improved light-harvesting capacity of TiO_2 catalysts. TiO_2 nanoparticles/Au nanobelts [25], Ag-Ag_2O/reduced TiO_2 [26], Ag nanoparticles@TiO_2 nanotubes [27], (Au, Ag, Cu and Pt)/anatase particles [28], Au/TiO_2 nanowires [29], Au-decorated ZnO [30] and ZnO–Au–SnO_2 [31] have been proved to be the efficient photocatalysts. To realize the low recombination rate, Yang and coworkers [32] used graphene as electron trap for promoting the separation of electron-hole pairs. One-dimensional electron transport channel also turns out to be helpful for the efficient separation according to the research results reported previously. The usage of carbon nanotubes as the electron traps in the CNT/TiO_2 composite resulted in the effective separation of electron-hole pairs and an improved photocatalytic performance [33–35].

However, most of the efforts reported can only improve either the separation of electron-hole pairs or the light-harvesting capacity of TiO_2-based catalysts. The fabrication of composite photocatalysts with both low recombination rate and enhanced light-harvesting capacity would be feasible for achieving superior photocatalytic performance. Ag nanowires should be a good choice owing to its SPR effect and high conductivity. Herein, an Ag nanowires@TiO_2 core–shell heterostructure with enhanced photocatalytic ability was synthesized by a facile one-step solvothermal treatment. Compared with bare TiO_2 catalyst, an enhanced removal ratio of gaseous acetaldehyde was observed when applying the Ag nanowires@TiO_2 core–shell heterostructure as photocatalyst. The related highest decomposition rate constant ($0.71959\ h^{-1}$) is almost 2.6 times larger than that of bare TiO_2 ($0.27739\ h^{-1}$). In the purpose of understanding the decomposition mechanism of acetaldehyde and effect of Ag nanowires, ESR tests and scavenge experiments were carried out. The coupling with Ag nanowires would benefit the generation of $\cdot O_2^-$, which was found to be essential for the photodecomposition of gaseous acetaldehyde. The in-depth mechanism proposed in this work would shed light on the further optimization of TiO_2-based photocatalysts and the effective decomposition of gas pollutants.

2. Experimental

2.1. Materials

Ag nanowires were purchased from Zhejiang Kechuang Advanced Materials Technology Co. Ltd. Tetrabutyl Titanate (TBOT) was purchased from Sinopharm Chemical Reagent Co. Ltd. p-benzoquinone (PBQ) and 2,2,6,6-tetramethyl-1-piperidinyloxy (TEMPO) were purchased from Aladdin Industrial Corporation. Deionized water was used.

2.2. The synthesis of Ag nanowires@TiO_2 core–shell heterostructure photocatalyst

In a typical process, 0.875 mg, 1.75 mg, 2.625 mg Ag nanowires were dispersed in 30 mL ethanol and 1 mL DI water by ultrasonication for 1 h. 1.5 mL TBOT was then added dropwise into the above mixture under magnetic stirring. The mixture was transferred into a 50 mL Teflon-lined autoclave and aged at 160 °C for 10 h. Afterwards, the suspension was centrifuged and washed with ethanol for several times. The obtained precipitates were dried in a vacuum oven overnight to obtain powder samples. The as-prepared samples were labeled as A0.25 T, A0.5 T, A0.75 T, where A stands for Ag nanowires and T for TiO_2, while 0.25, 0.5, 0.75 represent the mass ratio of Ag nanowires to TiO_2 are 0.25%, 0.5%, 0.75%, respectively. Bare TiO_2 was synthesized without adding Ag nanowires and denoted as A0T.

2.3. Characterization

X-ray diffraction (XRD) patterns were obtained on a D8 ADVANCE X-ray diffractometer (BRUKER AXS GMBH, German) with Cu Ka radiation (λ = 0.15418 nm, 2θ varied from 20° to 80°, 8°/min), the mode is continuous, the voltage is 40 kV, the current is 40 mA. UV–Vis spectra were collected on a Perkin–Elmer Lambda 950 spectrometer (250–800 nm). The Brunauer–Emmett–Teller (BET) specific surface area (S_{BET}) of the samples was analyzed by a Micromeritics ASAP 3000 nitrogen adsorption apparatus (All the samples were degassed at 120 °C for 5 h before nitrogen adsorption measurements were taken).The photoluminescence (PL) spectra were recorded on a Perkin–Elmer Luminescence spectrometer 55 (LS55) at an excited wavelength of 320 nm, the emission and excitation slitwidth are both 5 nm, and the scanning rate is 500 nm/min, the PL measurements were performed in powder. Fourier transform infrared spectroscopy (FTIR) spectra were measured by a Thermofisher iN10 iZ10 infrared spectrophotometer with a KBr pellet technique. Raman spectra were collected on a Thermal Dispersive Spectrometer using a laser with an excitation wavelength of 532 nm at laser power of 7 mW. The surface morphology of as-prepared powder was analyzed by using a field-emission scanning electron microscopy (FESEM) equipped with an Energy Dispersive Spectrometer (EDS) (FESEM, Magellan 400) (Firstly, powder was dispersed in ethanol by ultrasonication for 5 min. And then, the mixture was dropped on the

surface of Al foil. After natural drying, the Al foil was sticked to the platform by water-based conductive adhesive). The detailed microstructure of the product was analyzed by using a JEM-2100 HRTEM (JEOL) at an operating voltage of 200 kV (Firstly, powder was dispersed in ethanol by ultrasonication for 5 min. And then, the Cu grid was immersed in the mixture for 5 s. After natural drying, the Cu grid was placed on the holder). X-ray photoelectron spectroscopy (XPS) experiments were carried out on a RBD upgraded PHI-5000C ESCA system (Perkin Elmer) with MgKα radiation (1253.6 eV).

2.4. ESR test

Electron spin resonance (ESR) signal of active radicals trapped by 5,5-dimethyl-1-pyrroline N-oxide (DMPO) was recorded on a JES-FA200 spectrometer. 5,5-dimethyl-1-pyrroline N-oxide was purchased from DOJINDO Laboratories with purity higher than 99% as claimed from the producer. Samples for ESR measurements were prepared by mixing 4 mg sample with a solution containing 30 μL DMPO and 2 mL dispersion liquid (deionized water dispersion for DMPO-·OH and methanol dispersion for DMPO-$\cdot O_2^-$) under a 500 W Xe lamp irradiation with a 380 nm filter. The irradiation intensity was 30 mW/cm^2.

2.5. Photo-current response test

Photo-current response of the as-prepared samples was evaluated using a CHI660D electrochemical workstation in a conventional three-electrode quartz cell. Before the measurement, the sample was coated on a FTO glass by spin coating, and then the FTO disk acted as work electrode along with a platinum plate and an Ag/AgCl electrode as the counter and reference electrodes, respectively. The photo-current time curves were measured at 0.2 V versus Ag/AgCl in 1 mol/L Nacl at ambient temperature and an AM1.5G solar power system was used as light irradiation source.

2.6. Evaluation of photocatalytic activity

The photocatalytic activity experiments were tested by decomposing gaseous acetaldehyde in continuous flow reactor system at ambient temperature. The sealed photo-reactor was a 120 mL cuboid quartz vessel (15 cm × 8 cm × 1 cm). The 260 W fluorescent lamp was used as light irradiation source. The distance between the sample and the lamp was 20 cm and the light intensity was 20 mW/cm^2. The concentration of acetaldehyde was measured by gas chromatography, the schematic of the adsorption and photocatalytic process was shown in Fig. S1. The adsorption–desorption curves were displayed in Fig. S2, and the corresponding adsorption process was also described in detail. Firstly, the photocatalyst (0.1 g) was coated onto a glass slide (12 cm × 5 cm). The glass pane coated with photocatalyst was kept in dark for 180 min to reach an adsorption–desorption equilibrium. The initial concentration of acetaldehyde after adsorption–desorption equilibrium was fixed at 500 ± 10 ppm for all experiments, and the corresponding flow rate was controlled at 20 sccm. After that, the 260 W fluorescent lamp was turned on. The removal ratio (η) of acetaldehyde was calculated as $\eta = (1 - C/C_0) \times 100\%$, where C_0 is the initial concentration and C is the concentration of acetaldehyde at different time intervals, respectively. In addition, the contact time between the flowing acetaldehyde gas and the catalysts was calculated to be 4.8 min. (contact time = 120 mL/20 sccm * 12 cm/15 cm = 4.8 min).

2.7. Scavenger experiments

P-benzoquinone (PBQ) and 2,2,6,6-tetramethyl-1-piperidinyloxy (TEMPO) were applied to quench the corresponding superoxide radicals ($\cdot O_2^-$) and hydroxyl radicals (·OH) of A0.5 T. For the quenching of ($\cdot O_2^-$), the photocatalyst (0.1 g) was coated onto a glass slide (12 cm × 5 cm) by mixing additional 0.01 g PBQ together, and denoted as "A0.5 T + PBQ". Similarly, the photocatalyst (0.1 g) was mixed with 0.01 g TEMPO for the quenching of ·OH, and denoted as "A0.5 T + TEMPO". For comparison, the photocatalyst (0.1 g) was also mixed with 0.01 g PTFE powder, and denoted as "A0.5 T + No scavenger".

3. Results and discussion

3.1. Characterization of chemical composition and morphology

To investigate the phase structure of the as-synthesized Ag@TiO_2 composite materials, XRD and Raman measurements were conducted.

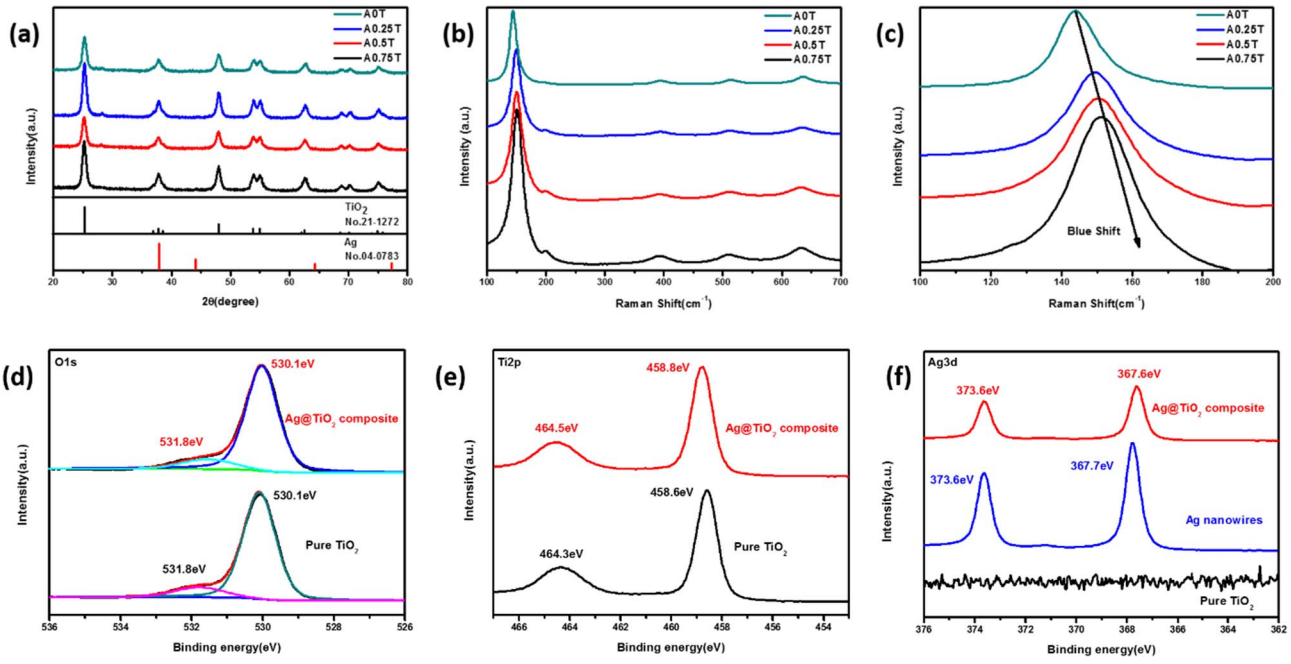

Fig. 1. (a) XRD patterns of the as-prepared samples with a scan speed of 8° min^{-1} (b) Raman spectra with an excitation wavelength of 532 nm at laser power of 7 mW (c) The enlarged Raman spectra at 144 cm^{-1} (d–f) X-ray photoelectron spectroscopy (XPS) spectra of O1s, Ti2p, Ag3d with MgKα radiation (1253.6 eV), respectively.

As shown by the XRD patterns in Fig. 1a, the characteristic peaks found in A0T, A0.25 T, A0.5 T, A0.75 T could be ascribed to anatase phase TiO_2 crystal (JCPDS No. 21-1272). No Ag characteristic peaks were found in the XRD patterns, and then the scanning rate of XRD was reduced from $8^\circ\,min^{-1}$ to $2^\circ\,min^{-1}$ for higher accuracy. As shown in Fig. S3, there were still no Ag characteristic peaks. This could be explained by the low Ag nanowires content in the composites [36]. Fig. 1b gives the Raman spectra of the Ag@TiO_2 composite materials. Raman bands located at 144, 197, 399, 519 and 639 cm^{-1} observed in the spectra could correspond to the E_g, E_g, B_{1g}, A_{1g}, and B_{1g} active modes of anatase TiO_2, respectively [37,38]. XRD and Raman results indicated that the anatase phase was the main phase in both bare TiO_2 nanoparticles and the composites. Compared with the Raman spectrum of bare TiO_2, a noticeable blueshift of around 10 cm^{-1} was found in the spectra of Ag@TiO_2 composites (Fig. 1c), which indicated the existence of lattice distortions or residual stress at the interface of Ag nanowires and TiO_2 nanoparticels owing to the lattice mismatch between them. It's an evidence of the close coupling between Ag nanowires and TiO_2 [39].

In order to confirm the formation of Ag@TiO_2 composites, XPS tests with high sensitivity were performed to give the elemental composition and the chemical status of the composite materials. All the binding energy values were calibrated by using C1s = 284.8 eV as a reference (Fig. S4). As shown in Fig. 1d, for both bare TiO_2 and Ag nanowires@TiO_2 composite, there is no distinct difference in the XPS spectra of O1s. Two XPS peaks located at 530.1 eV, 531.8 eV were observed in the O1s XPS spectra (Fig. 1d). The peak at 530.1 eV could be assigned to the Ti-O bonds in TiO_2 crystal lattice, and the peak at 531.8 eV could be ascribed to the Ti-OH bonds resulting from the hydroxyl groups on TiO_2 surface [40,41]. The Ti2p XPS peaks (Fig. 1e, Ag@TiO_2 composite) centered at 458.8 eV and 464.5 eV correspond to the $Ti2p_{3/2}$ and $Ti2p_{1/2}$ states of the Ti^{4+}-O bonds, and there was a 0.2 eV shift in comparison to that of pure TiO_2. As suggested by Fig. 1e, Ti^{4+} was the main form since no other valence of Ti element such as Ti^{3+} or Ti^{2+} existed in both bare TiO_2 and Ag nanowires@TiO_2 composites [42]. No peak was found in the Ag3d XPS spectrum of bare TiO_2 (Fig. 1f), while the Ag nanowires@TiO_2 composite consists of two peaks settled at 367.6 eV and 373.6 eV, which can be ascribed to $Ag3d_{3/2}$ and $Ag3d_{5/2}$ of the metallic silver, respectively [43,44]. Compared with the XPS of Ag

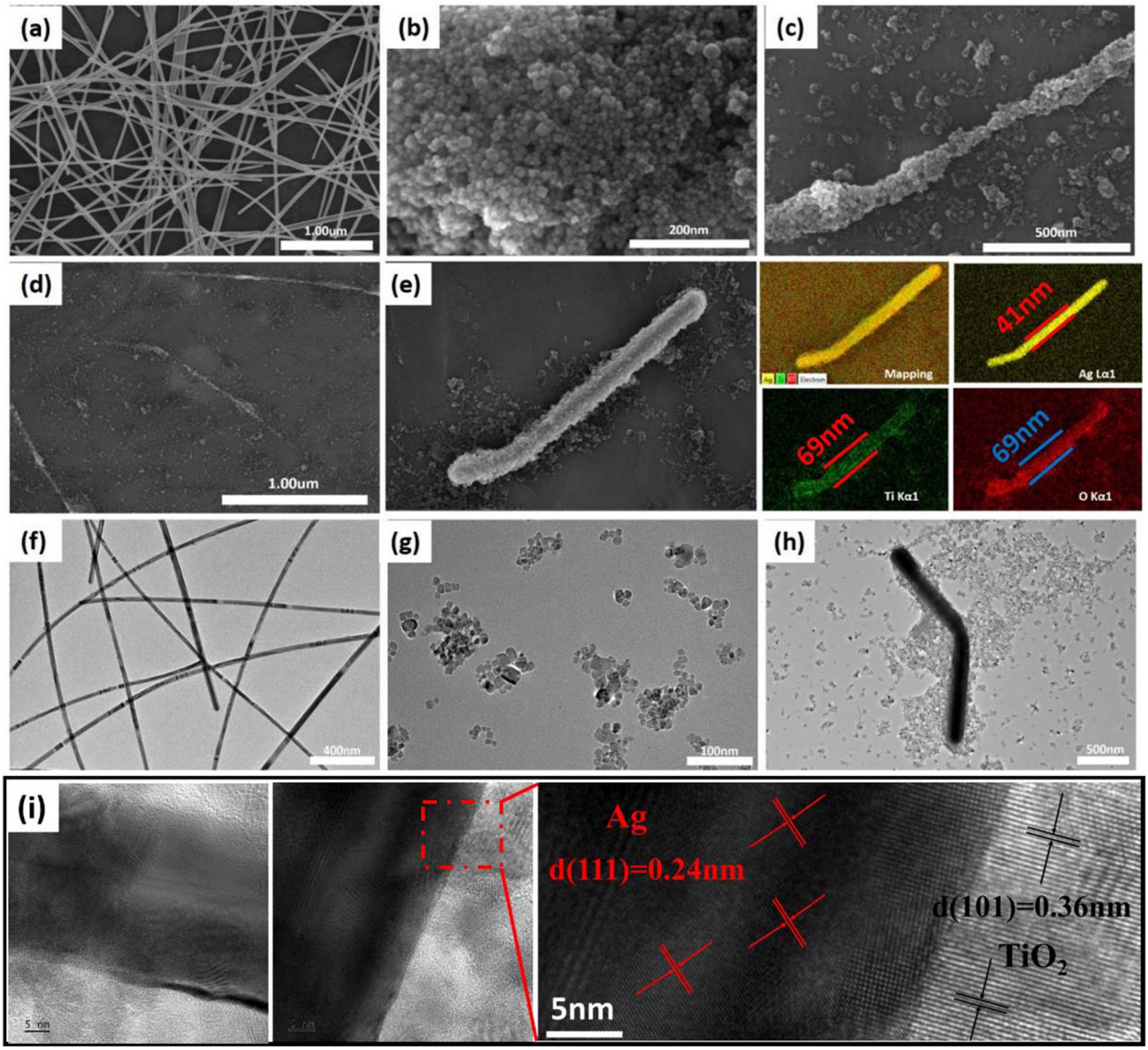

Fig. 2. (a) SEM image of pure Ag nanowires (b) SEM image of bare TiO_2 (c, d) SEM images of A0.25 T and A0.5 T (e) EDS elemental mapping images of Ag, Ti and O, respectively (f) TEM image of pure Ag nanowires (g) TEM image of bare TiO_2 (h) TEM image of Ag nanowires@TiO_2 core-shell composite (i) HRTEM images of the interface between Ag nanowires and TiO_2 nanoparticles.

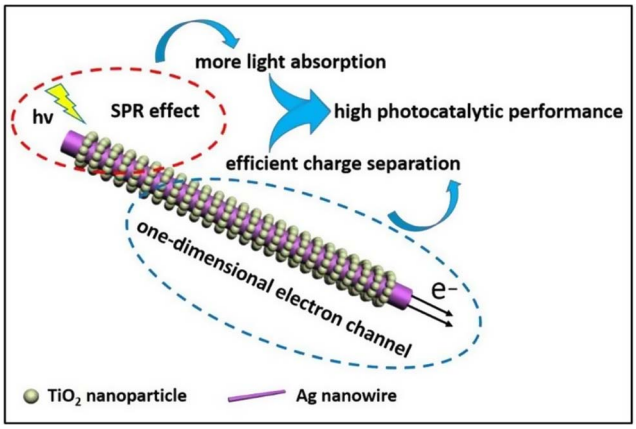

Scheme 1. The graphic illustration of one-dimensional core-shell structure.

nanowires, a 0.1 eV shift was observed from $Ag3d_{3/2}$ of the composites (Fig. 1f). The 0.2 eV shift of Ti2p and 0.1 eV shift of Ag3d both suggested a close interaction between TiO_2 nanoparticles and Ag nanowires. Concrete evidences on the co-existence of Ag and TiO_2 in the as-prepared composites was given by the XPS measurement results.

Similarly, in the FTIR spectrum (Fig. S5), the peak located at 3419 cm^{-1} was attributed to the stretching vibrations of O—H bond in absorbed water molecules [45]. The peak centered at 1630 cm^{-1} was assigned to the bending modes of water molecules [46]. The bands settled at 581 cm^{-1} and 647 cm^{-1} were associated with the bridge stretching modes of Ti-O and Ti-O-Ti bond in TiO_2 lattice [47]. These results were in accordance with the XRD and XPS analysis.

SEM images give the morphology of pure Ag nanowires, bare TiO_2 and Ag nanowires@TiO_2 composites. As displayed in Fig. 2a, Ag nanowires with smooth surface and a one-dimensional structure could be clearly seen. The average diameter was calculated to be ca. 40–50 nm (Fig. S6). Fig. 2b shows that the bare TiO_2 is consisted of multiple ultrafine nanoparticles with particle sizes of about 10–20 nm (Fig. S7). As revealed in Fig. 2c, d, the Ag nanowires@TiO_2 composites have a one-dimensional structure, with enlarged diameter and shortened length compared with Ag nanowires [43]. TiO_2 nanoparticles were deposited uniformly alongside the Ag nanowires, which caused an increase in their average diameter. Ag nanowires with an average length of 20 μm were cut into short nanowires (average lengths 2 μm) due to the corrosion caused by the harsh hydrothermal synthesis environment (Fig. S8). The EDS elemental mapping analysis was carried out to study the distribution of the Ag, Ti and O elements and reveal the one-dimensional structure of Ag@TiO_2 composites. The Ag nanowires core (with a diameter of around 41 nm) and the TiO_2 shell (with a thickness of around 15 nm) could be observed in Fig. 2e, indicating that the composites have a Ag nanowires@TiO_2 core–shell structure. No obvious changes in the Ag nanowires@TiO_2 heterostructures were observed when increasing the amount of Ag nanowires (Fig. S9, A0.75 T). Similar results were obtained from the TEM images (Fig. 2f–h). HRTEM was conducted to observed the incorporation of the interface between Ag nanowires and TiO_2 nanoparticels. As shown in Fig. 2i, the lattice fringe spacing of 0.24 nm was ascribed to the (1 1 1) plane of Ag, while the lattice fringe spacing of 0.36 nm corresponded to the (1 0 1) plane of anatase TiO_2. A clear overlap of the lattice boundaries between Ag and TiO_2 was observed. In a word, the synthesized composites were in one-dimensional core–shell structure which was clearly clarified by SEM and TEM. The related graphic illustration was shown in Scheme 1, the Ag nanowires core can interact with incident light due to its strong SPR effect, leading to more light absorption [22,23]. Meanwhile, the one-dimensional structure could further accelerate the transfer of electrons from TiO_2 to Ag nanowires, resulting in the efficient separation of electron-hole pairs [5,32]. In other words, this Ag@TiO_2 core–shell structure was beneficial to high photocatalytic performance.

3.2. The influence factors of photocatalytic performance

In the purpose of understanding the optical and electrical properties of the Ag nanowires@TiO_2 core–shell composites, UV–Vis spectra and PL spectra were tested. Fig. 3a gives the light-absorbing properties of bare TiO_2 and Ag nanowires@TiO_2 core–shell structures. High light absorbing abilities could be observed in the ultraviolet range (wavelength lower than 400 nm) for both bare TiO_2 and Ag nanowires@TiO_2 composites, which was in accordance with the strong light absorption of TiO_2 in the short wavelength range. However, differences could be observed in the visible range. Unlike bare TiO_2, the Ag nanowires@TiO_2 composites exhibited strong light-absorbing ability in the visible range with absorption peaks at around 450 nm. This could be attributed to the SPR effect of Ag nanowires. It is noteworthy that pure Ag nanowires show a SPR peak at 370 nm (Fig. 3a), while the composites show a SPR peak at 450 nm (Fig. 3a). This obvious redshift of SPR peak (370 nm to 450 nm) arises from the strong interfacial electronic coupling between Ag nanowires and TiO_2 [48]. To exclude the influence of the higher refractive index of TiO_2 than the surrounding medium on the SPR peak shift of Ag@TiO_2. The UV–Vis spectra of the sample ("0.75%Ag + TiO_2, physical mixing") was conducted. As shown in Fig. S10, there were no SPR peaks compared with A0.75 T and Ag nanowires. Namely, the higher refractive index of TiO_2 than the surrounding medium do not make any contribution to the SPR peak shift. Through broadening the light-absorbing capability of TiO_2 based catalysts to the visible range by adding small amount of Ag nanowires, composite photocatalysts with enhanced light-harvesting capacity was achieved, which was essential for the fabrication of highly-efficient photocatalysts.

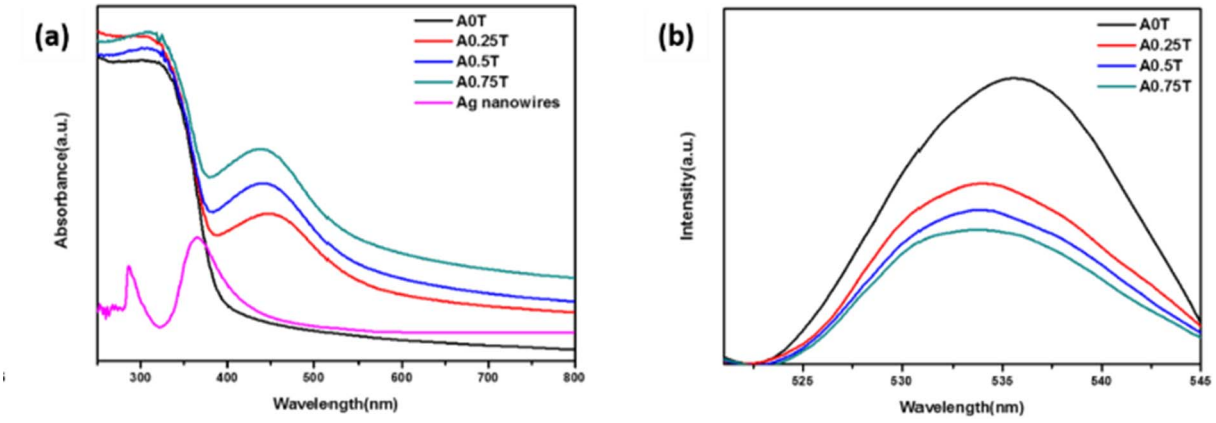

Fig. 3. (a) UV–Vis spectra of as-prepared samples, Ag nanowires (b) PL spectra at an excitation wavelength of 320 nm.

Apart from the light-harvesting capability, the recombination rate of photoinduced electron-hole pairs is another important factor that may affect the photocatalysis ability of TiO_2 based catalysts. The photoluminescence emission spectra (PL) was tested to evaluate the recombination behaviour of the photoinduced electron-hole pairs in both bare TiO_2 and Ag nanowires@TiO_2 composites. Compared with bare TiO_2 (A0T), the composites (A0.25 T, A0.5 T, A0.75 T) exhibited much lower PL intensity (Fig. 3b). The PL intensity could represent the recombination rate of photoinduced electron-hole pairs. The much lower PL intensity of the composite catalysts indicated that the existence of Ag nanowires would effectively prolong the lifetime of photoinduced electrons and holes and facilitate their utilization in the catalytic process. This phenomenon can be explained by the superior conductivity and the relative lower fermi level (0.4 V vs NHE [49]) of Ag nanowires (compared with the conduction band of TiO_2, −0.2 V vs NHE [13]). As one of the best conductors, Ag nanowires have shown superior ability in collecting and transporting electrons. The close combination between Ag nanowires and TiO_2 nanoparticles and the relative low Fermi level of Ag enabled the readily transfer of photoexcited electrons from TiO_2 to Ag nanowires [50], leaving the photoinduced holes in the valence band of TiO_2. The one-dimensional structure could also accelerate the movement of electrons along the Ag nanowires, which would further benefit the seperation of photoinduced electrons and holes. The efficient charge separation and lower recombination rate, which is induced by the unique Ag nanowire@TiO_2 core–shell heterostructure, would benefit the photocatalytic efficiency of the composite catalysts.

In addition to the light-harvesting capability and recombination rate, the specific surface area of photocatalysts could also influence their photocatalytic performance by affecting the adsorption of gas pollutant onto the surface of catalysts. N_2 adsorption analysis were performed to give the specific surface areas of the composite materials. The S_{BET} area was measured for three times. The specific values were listed in Table S1. The average S_{BET} was listed in Table 1, the corresponding S_{BET} area is 112.48 m^2/g, 108.94 m^2/g, 105.93 m^2/g, 99.82 m^2/g for A0T, A0.25 T, A0.5 T, A0.75 T, respectively. As the amount of Ag nanowires increased from 0 to 0.75%, a decrease of 11.3% was observed in the S_{BET} of composites catalysts, which might be caused by the agglomeration of TiO_2 around Ag nanowires. The addition of Ag nanowires has a slight negative effect on the S_{BET} of TiO_2 based catalysts, which would lead to the weaker adsorption of gas pollutants on the surface of catalysts, the generation of less active sites and the lower removal ratio of pollutants. In addition, the adsorption amount of acetaldehyde could be calculated by the adsorption–desorption curve (Fig. S2). The detailed computational process was displayed in Fig. S11. As shown in Table 1, the adsorption amount of acetaldehyde is 345.8 mL, 314.2 mL, 222.8 mL, 159.4 mL for A0T, A0.25 T, A0.5 T, A0.75 T, respectively. Although S_{BET} values were similar, there was a huge distinction in the adsorption amount of acetaldehyde. The differences between S_{BET} and the adsorptive properties resulted from the inequality between N_2 adsorption and acetaldehyde adsorption. In other words, the adsorptive property of acetaldehyde could reflect the effective reactive sites more straight in comparison to S_{BET}. The distinct adsorptive properties have a negative effect on the photocatalytic performance with the increasing Ag content. The pros and cons of combining Ag nanowires with TiO_2 nanoparticles indicated the existence of an optimal proportion of Ag nanowires in the composite materials. Compared with the research results reported perviously (a S_{BET} decrease of 78%) [44], the loss of specific surface area here is much smaller, which could be attributed to the relative small amount of Ag nanowires applied. Unlike the photocatalytic decomposition of liquid pollutants, the application of photocatalysts in air purification faced the problems of low concentration and short residence time, which puts forward higher requirements for the adsorption ability of photocatalysts. The relative high S_{BET} would be essential for the effective photodecomposition of gaseous pollutants.

Table 1
S_{BET} and adsorptive properties of A0T, A0.25 T, A0.5 T, A0.75 T (All the samples were degassed at 120 °C for 5 h before nitrogen adsorption measurements were taken, the adsorption amount of acetaldehyde was calculated from Fig. S11).

Sample	A0T	A0.25 T	A0.5 T	A0.75 T
S_{BET} (m^2/g)	112.48	108.95	105.93	99.82
Adsorption Amount of Acetaldehyde (mL)	345.8	314.2	222.8	159.4

3.3. Photocatalytic activity measurements

The specific photocatalytic performance was evaluated by the removal ratio of gaseous acetaldehyde (Fig. 4a). All the composites (A0.25 T, A0.5 T, A0.75 T) exhibited better photocatalytic ability than bare TiO_2 (A0T). The specific photocatalytic removal ratios were 51%, 72% and 63% for A0.25 T, A0.5 T and A0.75 T, respectively. Among all the samples, A0.5 T shows the highest removal ratio of 72%, which is almost twice the removal ratio of A0T (37%). The corresponding pseudo-first-order kinetic model was built to further investigate the reaction kinetics. The reaction rate constant k was determined by using the equation: $-\ln(C/C_0) = kt$. As displayed in Fig. 4b, the calculated first-order kinetic constants were 0.27739 h^{-1}, 0.45678 h^{-1}, 0.71959 h^{-1}, 0.58973 h^{-1} for A0T, A0.25 T, A0.5 T, A0.75 T, respectively. The highest constant was observed for A0.5 T (0.71959 h^{-1}), which was almost 2.6 times larger than that of A0T (0.27739 h^{-1}). This was in good accordance with the gaseous acetaldehyde removal results. Besides, the removal ratio of gaseous acetaldehyde firstly increased (51% to 72%, A0.25 T to A0.5 T), and then declined (72% to 63%, A0.5 T to A0.75 T) with the addition of Ag nanowirs. The optimal proportion for Ag nanowires was found to be 0.5%, which could be easily explained by the synergistic effect of Ag nanowires on the light absorption (UV–Vis spectra, Fig. 3a), recombination rate (PL spectra, Fig. 3b), and reactive sites (S_{BET} area and adsorption amount of acetaldehyde, Table 1) of composite catalysts. On one hand, the S_{BET} area and adsorption amount of acetaldehyde were getting smaller with the increment of Ag nanowires content (Table 1), which led to a lose in the photocatalytic activity of TiO_2 photocatalysts. Additionally, Hsu's group [51,52] studied the influence of the excessive metal loading on emission lifetime by time-resolved PL spectra, it turns out that the excessive metal loading which acted as charge recombination center can cause the emission lifetime shortening. Therefore, this may be another disadvantage of too much Ag loading. On the other hand, with the increasing Ag nanowires content, higher light-harvesting capacity and lower recombination rate (Fig. 3a, b) could be achieved, which is beneficial to the optimization of the catalyst. In short, the competition between the negative and positive effect of Ag nanowires on the photocatalytic performance of composite catalysts explained the existence of an optimal Ag nanowires ratio.

However, it is nonnegligible that the improvement of photocatalytic performance here is not satisfactory enough. As is well-known, in the photodegradation of liquid organic dyes, photocatalytic performance can usually be increased several times or even dozens of times. Here is the reason: compared with the as long as several hours contact time of liquid photocatalysis, the contact time between the flowing acetaldehyde gas and the catalysts was quite short (4.8 min). So, it is easy to understand that photocatalytic performance improvement here was just twice (37% to 72%, A0T to A0.5 T).

In addition, two comparative experiments were conducted to ensure that pure Ag nanowires and light have no contribution to the gaseous acetaldehyde decomposition. The first one was conducted by applying pure Ag nanowires as the photocatalyst with other experiment conditions unchanged. The result (Fig. S12) showed pure Ag nanowires have no photocatalytic activity. The second one was carried out without any photocatalysts but only the light applied. As revealed in Fig. S13, the

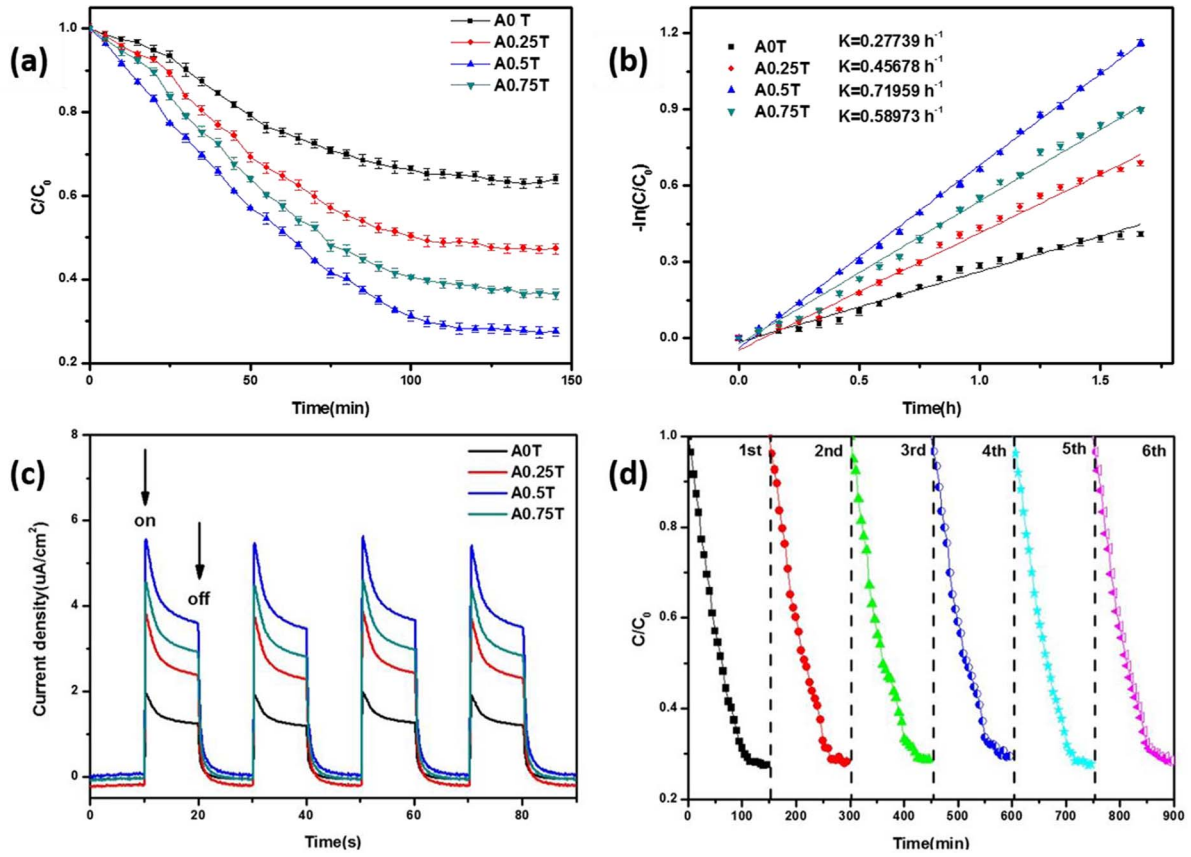

Fig. 4. (a) The photodecomposition ratio for gaseous acetaldehyde with a 260 W fluorescent lamp as light source (b) Corresponding pseudo-first-order kinetic model of as-prepared samples (c) Photo-current response of as-prepared samples (d) Cyclic experiments with A0.5 T.

light showed no photolysis effect on acetaldehyde either. This two comparative experiments indicated that pure Ag nanowires and light do not make any contribution to the decomposition of gaseous acetaldehyde.

We also measured the photo-current response of the as-prepared samples through a three-electrode system under the AM1.5G illumination. A rapid photo-current response was observed for all of the samples (Fig. 4c). A gradual decay could be found in each individual switch-on/off process, which implied that the photoinduced electron-hole pairs are undergoing a recombination process [5]. The photo-current response exhibited excellent repeatability in four light on/off cycles, which implied the outstanding chemical stability of composite catalysts [37]. The relatively larger photo-current densities were realized for all Ag nanowires samples (A0.25 T, A0.5 T, A0.75 T) in comparison to bare TiO_2 (A0T). In general, the photocatalytic activity can also be reflected by the corresponding photo-current density [53]. It is clear that the composite catalysts possess not only excellent photocatalytic behaviour but also charming chemical stability.

In consideration of practical application, the reusability is another important criteria when evaluating photocatalysts. Cyclic experiments for the photocatalytic removal of gaseous acetaldehyde with A0.5 T were carried out. The time interval between two cycles was 3 weeks. Fig. 4d illustrates the relationship between the gaseous acetaldehyde removal ratio and the cycling times. The photocatalysts could remain fairly high activity with no obvious decline after six cycles (15 weeks), which ensured the practical application of composite catalysts in the long-term usage.

3.4. Photocatalytic oxidation mechanism

To gain further insights on the photocatalytic process, electron spin resonance (ESR) tests were conducted to detect the generation of superoxide radicals ($\cdot O_2^-$) and hydroxyl radicals ($\cdot OH$) under the illumination of light [54,55]. The four characteristic peaks of both DMPO-$\cdot O_2^-$ (with a 1:1:1:1 area ratio) (Fig. 5a) and DMPO-$\cdot OH$ (with a 1:2:2:1 area ratio) (Fig. 5b) were observed in all samples. In both cases (superoxide radicals ($\cdot O_2^-$) or hydroxyl radicals ($\cdot OH$)), the signal intensities (Fig. 5a, b) of the composites (A0.25 T, A0.5 T, A0.75 T) are stronger in comparison to bare TiO_2 (A0T). A higher ESR signal intensity generally represents more reactive radicals, which is essential for better photocatalytic performance [56]. The strongest signal was achieved when the content of Ag nanowires was 0.5 wt% (A0.5 T). Compared with A0.75 T, A0.5 T has shown similar capability in the separation of photoinduced electron-hole pairs (Fig. 3b) but higher specific surface area (Table 1), which accounts for the higher concentration of active radicals. The result is in good agreement with the photocatalytic activity (Fig. 4a) and the photo-current response (Fig. 4c) of composite catalysts with different Ag nanowires-loading contents. But, it is worth noticing that the signals of superoxide radicals ($\cdot O_2^-$) are stronger than the ones of hydroxyl radicals ($\cdot OH$), which indicates that $\cdot O_2^-$ may play the predominant role in the photocatalytic process [57–59].

In the purpose of understanding the role of superoxide radicals and hydroxyl radicals, scavenger experiments were performed by applying A0.5 T as the photocatalyst. P-benzoquinone (PBQ) and 2,2,6,6-Tetramethyl-1-piperidinyloxy (TEMPO) were applied to quench the corresponding superoxide radicals ($\cdot O_2^-$) and hydroxyl radicals ($\cdot OH$) [1,56,60,61]. Excessive amount of scavenger reagents were utilized to guarantee the completely capture of related radicals. After the quenching of $\cdot O_2^-$ and $\cdot OH$ by PBQ and TEMPO, the related photocatalytic performance changed a lot. As revealed in Fig. 5c, when the $\cdot O_2^-$ was scavenged by PBQ, the removal ratio of acetaldehyde decreased from 73% to 26%, while the quenching of $\cdot OH$ caused a decline from 73% to 51%. The scavenger experiments results indicated that

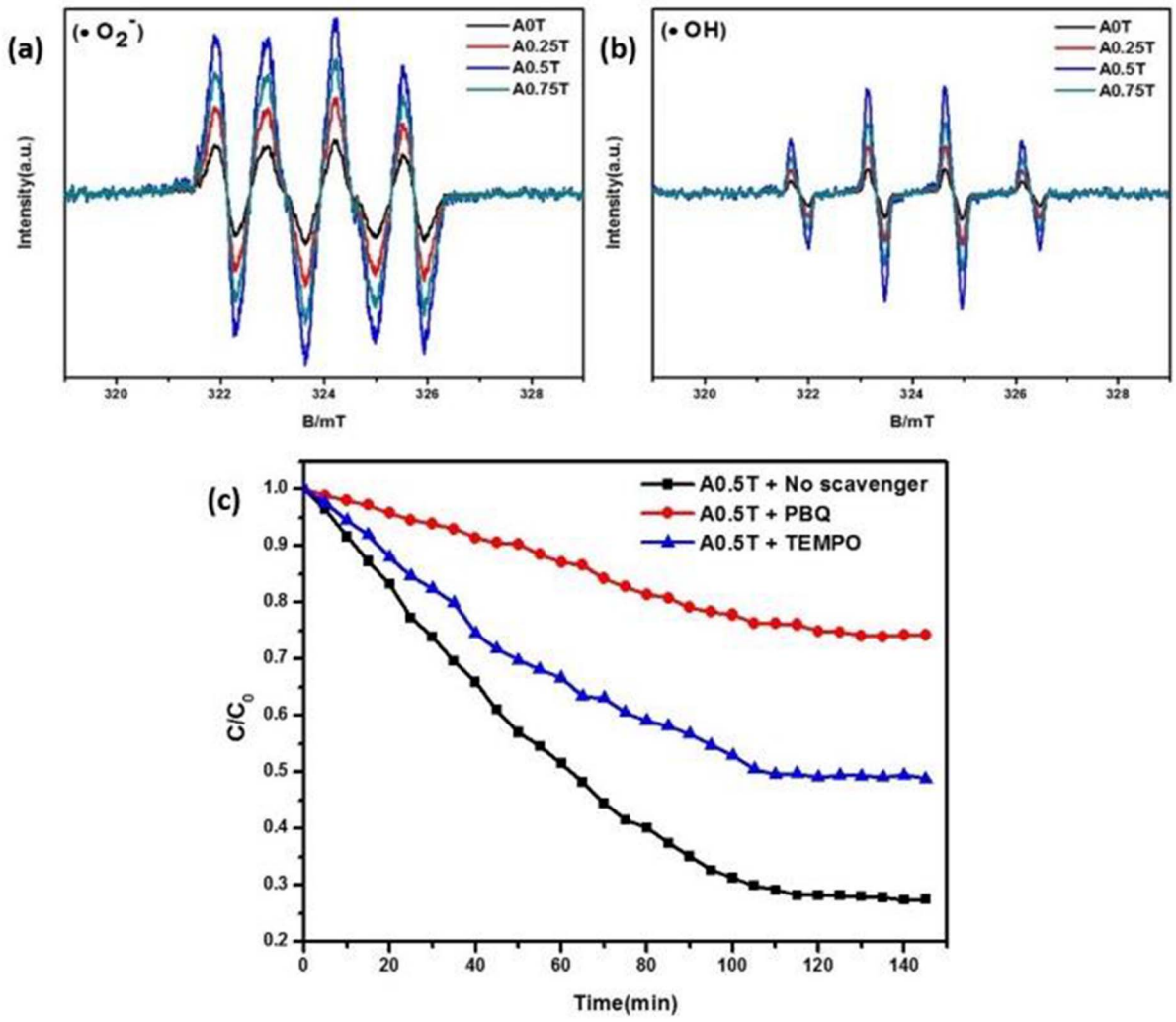

Fig. 5. (a) Superoxide radicals (˙O_2^-) signal with DMPO as scavenger in ethanol (b) Hydroxyl radicals (˙OH) signal with DMPO as scavenger in water (c) Scavenger experiments using PBQ and TEMO as corresponding ˙O_2^- and ˙OH quenching.

compared with ·OH radicals, ·O_2^- radicals do play a more important role in the photodecomposition of gaseous acetaldehyde. The results are in consistent with the aforementioned ESR results. Briefly, through combining ESR tests and scavenger experiments together, the two reactive radicals (·O_2^-, ·OH) were proved to play different roles in the photocatalytic process.

Finally, based on all the results, an in-depth mechanism (Scheme 2) was proposed to help us better understand the photodecomposition process of gaseous acetaldehyde. Under the stimulus of incident light, electrons would be excited to the conduction band (CB) of TiO_2. Due to the differences between the Fermi levels of Ag and the conduction band of TiO_2, these free electrons will flow to the Ag nanowires, leaving the holes at the valence band of TiO_2. The interaction between electrons and oxygen led to the generation of superoxide radicals (·O_2^-) while hydroxyl radicals (·OH) were generated through the reaction between photoinduced holes and water. Gaseous acetaldehyde adsorbed on the surface of the photocatalyst would then be decomposed by the active radicals through the following paths (Scheme 2). A small part of acetaldehyde could be oxidized into carbon dioxide and water directly by ·O_2^- or ·OH (step A or B, $CH{-}3CHO \xrightarrow{\cdot O_2^-/\cdot OH} CO_2 + H_2O$, Scheme 2) [62]. The rest was firstly oxidized into acetic acid by ·OH (step C, $CH{-}3CHO \xrightarrow{\cdot OH} CH_3COOH$, Scheme 2) [63], and then oxidized into carbon dioxide and water by ·O_2^- (step D, $CH_3COOH \xrightarrow{\cdot O_2^-} CO_2 + H_2O$, Scheme 2) [64]. As mentioned before, the photocatalytic performance changed a lot after the quenching of ·O_2^-, but changed a little after the quenching of ·OH (Fig. 5c). That is, ·O_2^- is the predominant reactive radicals, while ·OH is the secondary reactive radicals. Therefore, the higher photocatalytic performance could be realized through anchoring −OH, −COOH or oxygen vacancies on the surface of TiO_2-based photocatalysts, which are conducive to the generation of ·O_2^-. In other words, the in-depth understanding of the photodecomposition mechanism casts light on the further optimization of TiO_2-based catalysts.

4. Conclusions

In summary, the Ag nanowires@TiO_2 core–shell nanostructures were synthesized via a facile one-step solvothermal process. Benefitting from the unique one-dimensional core–shell heterostructure, the composite catalysts exhibited improved light-harvesting capability and efficient charge separation, as well as the relative high S_{BET}, which made them great candidates for the photodecomposition of gaseous pollutants. Through applying the as-synthesized composite catalysts in the photodecomposition of acetaldehyde, an improved removal ratio of 72% (A0.5 T) (nearly twice the removal ratio of bare TiO_2) was achieved, although the contact time was very short (4.8 min). Besides, it is found that the adsorptive property could reflect the effective reactive sites more straight in comparison to S_{BET} for gaseous pollutants adsorption. The photocatalyst also preserved ultrastable activity in the 15 weeks usage, which ensures the practical application of Ag

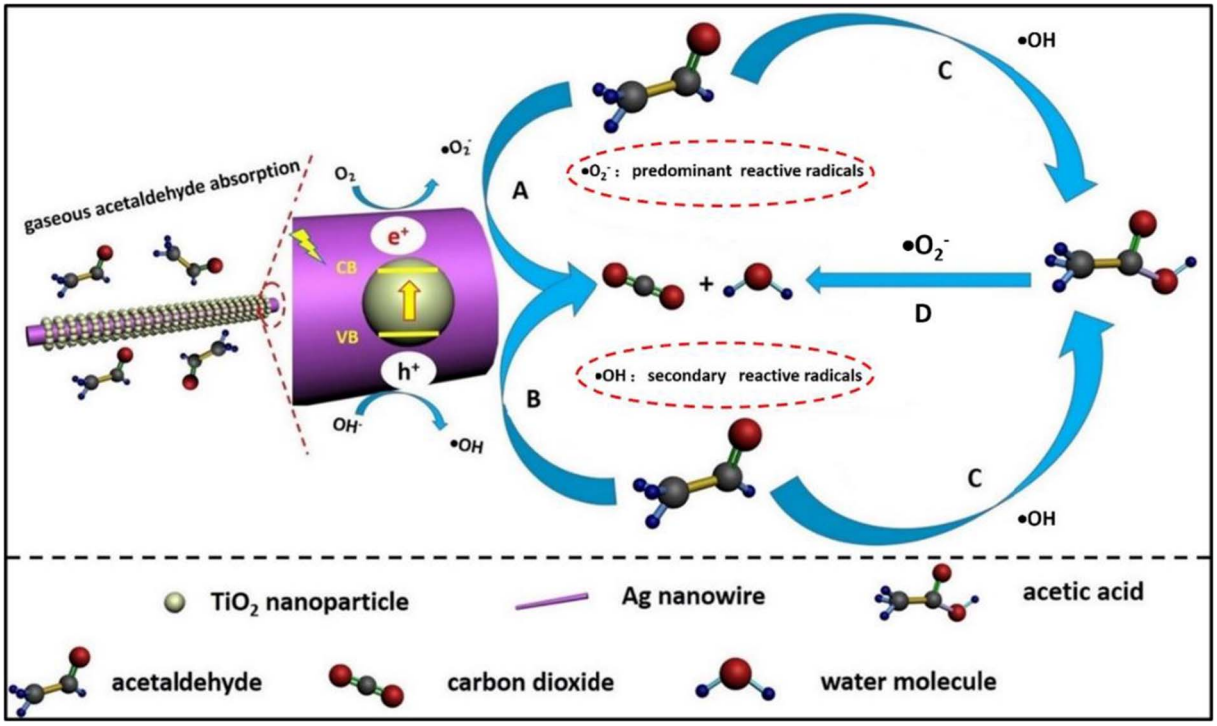

Scheme 2. Schematic of the whole photocatalytic process for gaseous acetaldehyde decomposition.

nanowires@TiO_2 composite catalysts. This work indicates that constructing other similar one-dimensional core–shell structure would be an alternative way to realize efficient photocatalysis. Besides, the generation of active radicals (superoxide radicals and hydroxyl radicals) and their roles in the photodecomposition of acetaldehyde were characterized through ESR tests and scavenger experiments. $\cdot O_2^-$ radicals were found to play a predominant role in the decomposition of acetaldehyde. On the basis of the research results, an in-depth discussion on the decomposition mechanism was given. The in-depth understanding of the photodecomposition mechanism enables the further optimization of TiO_2-based photocatalysts for the effective decomposition of gaseous pollutants.

Conflicts of interest

There are no conflicts to declare.

Acknowledgements

This work was financially supported by the National Key Research and Development Program of China (2016YFA0203000), the Key Project of International Cooperation of the Chinese Academy of Sciences (GJHZ1656), and the National Natural Science Foundation of China (No. 51702347).

Appendix A. Supplementary data

Supplementary data associated with this article can be found, in the online version, at http://dx.doi.org/10.1016/j.cej.2018.02.015.

References

[1] Z. Zhang, M. Xu, W. Ho, X. Zhang, Z. Yang, X. Wang, Simultaneous excitation of PdCl2 hybrid mesoporous g-C3N4 molecular/solid-state photocatalysts for enhancing the visible-light-induced oxidative removal of nitrogen oxides, Appl. Catal. B 184 (2016) 174–181.
[2] A.Y. Chen, S.S. Shi, F. Liu, Y. Wang, X. Li, J.F. Gu, X.F. Xie, Effect of annealing atmosphere on the thermal coarsening of nanoporous gold films, Appl. Surf. Sci. 355 (2015) 133–138.
[3] H. Liu, X. Dong, C. Duan, Z. Zhu, A simple fabrication of Ag-nanowires@TiO2 core-shell nanostructures for the construction of mediator-free biosensor, J. Solid State Electrochem. 19 (2014) 543–548.
[4] Y. Wang, L. Yan, X. He, J. Li, D. Wang, Controlled fabrication of Ag/TiO2 nanofibers with enhanced stability of photocatalytic activity, J. Mater. Sci.: Mater. Electron. 27 (2016) 5190–5196.
[5] C. Jia, P. Yang, J. Li, B. Huang, K. Matras-Postolek, Photocatalytic activity evolution of different morphological TiO_2 shells on Ag nanowires, ChemCatChem 8 (2016) 839–847.
[6] D.H. Wang, L. Jia, X.L. Wu, L.Q. Lu, A.W. Xu, One-step hydrothermal synthesis of N-doped TiO2/C nanocomposites with high visible light photocatalytic activity, Nanoscale 4 (2012) 576–584.
[7] X. Zhou, N. Liu, P. Schmuki, Photocatalysis with TiO2 nanotubes: “colorful” reactivity and designing site-specific photocatalytic centers into TiO2 nanotubes, ACS Catal. 7 (2017) 3210–3235.
[8] A.Y. Chen, S.S. Shi, J.W. Wang, F. Liu, F. Wang, Y. Wang, H.H. Ruan, X.F. Xie, Microstructure and electrocatalytic performance of nanoporous gold foils decorated by TiO2 coatings, Surf. Coat. Technol. 286 (2016) 113–118.
[9] M. Zeng, Y. Li, M. Mao, J. Bai, L. Ren, X. Zhao, Synergetic effect between photocatalysis on TiO2 and thermocatalysis on CeO2 for gas-phase oxidation of benzene on TiO2/CeO2 nanocomposites, ACS Catal. 5 (2015) 3278–3286.
[10] G. Li, L. Wu, F. Li, P. Xu, D. Zhang, H. Li, Photoelectrocatalytic degradation of organic pollutants via a CdS quantum dots enhanced TiO2 nanotube array electrode under visible light irradiation, Nanoscale 5 (2013) 2118–2125.
[11] W.Q. Han, L.J. Wu, R.F. Klie, Y.M. Zhu, Enhanced optical absorption induced by dense nanocavities inside titania nanorods, Adv. Mater. 19 (2007) 2525–2529.
[12] Y. Zhang, M. Huang, F. Li, H. Zhao, Z. Wen, Decoration of Cu nanowires with chemically modified TiO2 nanoparticles for their improved photocatalytic performance, J. Mater. Sci. 48 (2013) 6728–6736.
[13] H. Eom, J.Y. Jung, Y. Shin, S. Kim, J.H. Choi, E. Lee, J.H. Jeong, I. Park, Strong localized surface plasmon resonance effects of Ag/TiO2 core-shell nanowire arrays in UV and visible light for photocatalytic activity, Nanoscale 6 (2014) 226–234.
[14] B. Babu, K. Mallikarjuna, C.V. Reddy, J. Park, Facile synthesis of Cu@TiO2 core shell nanowires for efficient photocatalysis, Mater. Lett. 176 (2016) 265–269.
[15] X. Zhang, Y. Wang, B. Liu, Y. Sang, H. Liu, Heterostructures construction on TiO 2 nanobelts: A powerful tool for building high-performance photocatalysts, Appl. Catal. B 202 (2017) 620–641.
[16] Z. Shayegan, C.-S. Lee, F. Haghighat, TiO2 photocatalyst for removal of volatile organic compounds in gas phase – a review, Chem. Eng. J. 334 (2018) 2408–2439.
[17] X. Liu, J. Iocozzia, Y. Wang, X. Cui, Y. Chen, S. Zhao, Z. Li, Z. Lin, Noble metal–metal oxide nanohybrids with tailored nanostructures for efficient solar energy conversion, photocatalysis and environmental remediation, Energy Environ. Sci. 10 (2017) 402–434.
[18] Y. Boyjoo, H. Sun, J. Liu, V.K. Pareek, S. Wang, A review on photocatalysis for air treatment: from catalyst development to reactor design, Chem. Eng. J. 310 (2017) 537–559.
[19] J. Li, M. Zhang, X. Li, Q. Li, J. Yang, Effect of the calcination temperature on the

visible light photocatalytic activity of direct contact Z-scheme g-C3 N4 -TiO2 heterojunction, Appl. Catal. B 212 (2017) 106–114.
[20] N. Lu, C. Wang, B. Sun, Z. Gao, Y. Su, Fabrication of TiO2-doped single layer graphitic-C3 N4 and its visible-light photocatalytic activity, Sep. Purif. Technol. 186 (2017) 226–232.
[21] Y. Wen, H. Ding, Y. Shan, Preparation and visible light photocatalytic activity of Ag/TiO(2)/graphene nanocomposite, Nanoscale 3 (2011) 4411–4417.
[22] D. Tsukamoto, Y. Shiraishi, Y. Sugano, S. Ichikawa, S. Tanaka, T. Hirai, Gold nanoparticles located at the interface of anatase/rutile TiO2 particles as active plasmonic photocatalysts for aerobic oxidation, J. Am. Chem. Soc. 134 (2012) 6309–6315.
[23] Z. Bian, T. Tachikawa, P. Zhang, M. Fujitsuka, T. Majima, Au/TiO2 superstructure-based plasmonic photocatalysts exhibiting efficient charge separation and unprecedented activity, J. Am. Chem. Soc. 136 (2014) 458–465.
[24] J.B. Priebe, J. Radnik, A.J.J. Lennox, M.-M. Pohl, M. Karnahl, D. Hollmann, K. Grabow, U. Bentrup, H. Junge, M. Beller, A. Brückner, Solar hydrogen production by plasmonic Au–TiO2 catalysts: impact of synthesis protocol and TiO2 phase on charge transfer efficiency and H2 evolution rates, ACS Catal. 5 (2015) 2137–2148.
[25] Q. Chen, H. Liu, Y. Xin, X. Cheng, Coupling immobilized TiO2 nanobelts and Au nanoparticles for enhanced photocatalytic and photoelectrocatalytic activity and mechanism insights, Chem. Eng. J. 241 (2014) 145–154.
[26] Y. Cui, Q. Ma, X. Deng, Q. Meng, X. Cheng, M. Xie, X. Li, Q. Cheng, H. Liu, Fabrication of Ag-Ag2 O/reduced TiO2 nanophotocatalyst and its enhanced visible light driven photocatalytic performance for degradation of diclofenac solution, Appl. Catal. B 206 (2017) 136–145.
[27] M.Z. Ge, C.Y. Cao, S.H. Li, Y.X. Tang, L.N. Wang, N. Qi, J.Y. Huang, K.Q. Zhang, S.S. Al-Deyab, Y.K. Lai, In situ plasmonic Ag nanoparticle anchored TiO2 nanotube arrays as visible-light-driven photocatalysts for enhanced water splitting, Nanoscale 8 (2016) 5226–5234.
[28] Z. Wei, M. Endo, K. Wang, E. Charbit, A. Markowska-Szczupak, B. Ohtani, E. Kowalska, Noble metal-modified octahedral anatase titania particles with enhanced activity for decomposition of chemical and microbiological pollutants, Chem. Eng. J. 318 (2017) 121–134.
[29] Y.C. Pu, G. Wang, K.D. Chang, Y. Ling, Y.K. Lin, B.C. Fitzmorris, C.M. Liu, X. Lu, Y. Tong, J.Z. Zhang, Y.J. Hsu, Y. Li, Au nanostructure-decorated TiO2 nanowires exhibiting photoactivity across entire UV-visible region for photoelectrochemical water splitting, Nano Lett. 13 (2013) 3817–3823.
[30] Y.-H. Chiu, K.-D. Chang, Y.-J. Hsu, Plasmon-mediated charge dynamics and photoactivity enhancement for Au-decorated ZnO nanocrystals, J. Mater. Chem. A (2018).
[31] J.M. Li, H.Y. Cheng, Y.H. Chiu, Y.J. Hsu, ZnO-Au-SnO2 Z-scheme photoanodes for remarkable photoelectrochemical water splitting, Nanoscale 8 (2016) 15720–15729.
[32] N. Yang, Y. Liu, H. Wen, Z. Tang, H. Zhao, Y. Li, D. Wang, Photocatalytic properties of graphdiyne and graphene modified TiO(2): from theory to experiment, ACS Nano 7 (2013) 1504–1512.
[33] Y. Zhang, Z. Xing, J. Zou, Z. Li, X. Wu, L. Shen, Q. Zhu, S. Yang, W. Zhou, 3D urchin-like black TiO2−x/carbon nanotube heterostructures as efficient visible-light-driven photocatalysts, RSC Adv. 7 (2017) 453–460.
[34] Y. Panahian, N. Arsalani, Synthesis of hedgehog like F-TiO2(B)/CNT nanocomposites for sonophotocatalytic and photocatalytic degradation of malachite green (MG) under visible light: kinetic study, J. Phys. Chem. A 121 (2017) 5614–5624.
[35] D. Eder, A.H. Windle, Carbon-inorganic hybrid materials: the carbon-nanotube/TiO2 interface, Adv. Mater. 20 (2008) 1787–1793.
[36] Y. Wu, S. Yuan, R. Feng, Z. Ma, Y. Gao, S. Xing, Comparative study for low-temperature catalytic oxidation of o-xylene over doped OMS-2 catalysts: role of Ag and Cu, Mol. Catal. 442 (2017) 164–172.
[37] J.S. Lee, K.H. You, C.B. Park, Highly photoactive, low bandgap TiO2 nanoparticles wrapped by graphene, Adv. Mater. 24 (2012) 1084–1088.
[38] Z. Wang, C. Yang, T. Lin, H. Yin, P. Chen, D. Wan, F. Xu, F. Huang, J. Lin, X. Xie, M. Jiang, H-doped black titania with very high solar absorption and excellent photocatalysis enhanced by localized surface plasmon resonance, Adv. Funct. Mater. 23 (2013) 5444–5450.
[39] Z. Wang, C. Yang, T. Lin, H. Yin, P. Chen, D. Wan, F. Xu, F. Huang, J. Lin, X. Xie, M. Jiang, Visible-light photocatalytic, solar thermal and photoelectrochemical properties of aluminium-reduced black titania, Energy Environ. Sci. 6 (2013) 3007.
[40] X. Zhang, J. Wang, W. Hu, K. Zhang, B. Sun, G. Tian, B. Jiang, K. Pan, W. Zhou, Facile strategy to fabricate uniform black TiO2 nanothorns/graphene/black TiO2 nanothorns sandwichlike nanosheets for excellent solar-driven photocatalytic performance, ChemCatChem 8 (2016) 3240–3246.
[41] J. Liqiang, F. Honggang, W. Baiqi, W. Dejun, X. Baifu, L. Shudan, S. Jiazhong, Effects of Sn dopant on the photoinduced charge property and photocatalytic activity of TiO2 nanoparticles, Appl. Catal. B 62 (2006) 282–291.
[42] Q. Ke, C. Guan, X. Zhang, M. Zheng, Y.W. Zhang, Y. Cai, H. Zhang, J. Wang, Surface-charge-mediated formation of H-TiO2@Ni(OH)2 heterostructures for high-performance supercapacitors, Adv. Mater. 29 (2017).
[43] P. Ramasamy, D.-M. Seo, S.-H. Kim, J. Kim, Effects of TiO2 shells on optical and thermal properties of silver nanowires, J. Mater. Chem. 22 (2012) 11651.
[44] B. Cheng, Y. Le, J. Yu, Preparation and enhanced photocatalytic activity of Ag@TiO2 core-shell nanocomposite nanowires, J. Hazard. Mater. 177 (2010) 971–977.
[45] B. Qiu, M. Xing, J. Zhang, Mesoporous TiO2 nanocrystals grown in situ on graphene aerogels for high photocatalysis and lithium-ion batteries, J. Am. Chem. Soc. 136 (2014) 5852–5855.
[46] T. Xia, C. Zhang, N.A. Oyler, X. Chen, Hydrogenated TiO(2) nanocrystals: a novel microwave absorbing material, Adv. Mater. 25 (2013) 6905–6910.
[47] N. Riaz, F.K. Chong, B.K. Dutta, Z.B. Man, M.S. Khan, E. Nurlaela, Photodegradation of Orange II under visible light using Cu–Ni/TiO2: Effect of calcination temperature, Chem. Eng. J. 185–186 (2012) 108–119.
[48] C. Jia, H.-S. Chen, P. Yang, Selective growth of TiO2beads on Ag nanowires and their photocatalytic performance, CrystEngComm 17 (2015) 4895–4902.
[49] S. Fu, Y. He, Q. Wu, Y. Wu, T. Wu, Visible-light responsive plasmonic Ag2O/Ag/g-C3N4 nanosheets with enhanced photocatalytic degradation of Rhodamine B, J. Mater. Res. 31 (2016) 2252–2260.
[50] M. Ye, J. Gong, Y. Lai, C. Lin, Z. Lin, High-efficiency photoelectrocatalytic hydrogen generation enabled by palladium quantum dots-sensitized TiO2 nanotube arrays, J. Am. Chem. Soc. 134 (2012) 15720–15723.
[51] W.H. Lin, Y.H. Chiu, P.W. Shao, Y.J. Hsu, Metal-particle-decorated ZnO nanocrystals: photocatalysis and charge dynamics, ACS Appl. Mater. Interfaces 8 (2016) 32754–32763.
[52] Y.-H. Hsu, A.T. Nguyen, Y.-H. Chiu, J.-M. Li, Y.-J. Hsu, Au-decorated GaOOH nanorods enhanced the performance of direct methanol fuel cells under light illumination, Appl. Catal. B 185 (2016) 133–140.
[53] Z. Xu, J. Yu, Visible-light-induced photoelectrochemical behaviors of Fe-modified TiO2 nanotube arrays, Nanoscale 3 (2011) 3138–3144.
[54] W. Zhang, Y. Sun, F. Dong, W. Zhang, S. Duan, Q. Zhang, Facile synthesis of organic–inorganic layered nanojunctions of g-C3N4/(BiO)2CO3 as efficient visible light photocatalyst, Dalton Trans. 43 (2014) 12026–12036.
[55] M. Yang, Q. Yang, J. Zhong, S. Huang, J. Li, J. Song, C. Burda, Enhanced photocatalytic performance of Ag2O/BiOF composite photocatalysts originating from efficient interfacial charge separation, Appl. Surf. Sci. 416 (2017) 666–671.
[56] Z. Wang, Y. Huang, W. Ho, J. Cao, Z. Shen, S.C. Lee, Fabrication of Bi 2 O 2 CO 3 /g-C 3 N 4 heterojunctions for efficiently photocatalytic NO in air removal: In-situ self-sacrificial synthesis, characterizations and mechanistic study, Appl. Catal. B 199 (2016) 123–133.
[57] X. Li, S. Fang, L. Ge, C. Han, P. Qiu, W. Liu, Synthesis of flower-like Ag/AgCl-Bi2MoO6 plasmonic photocatalysts with enhanced visible-light photocatalytic performance, Appl. Catal. B 176–177 (2015) 62–69.
[58] C. Han, L. Ge, C. Chen, Y. Li, X. Xiao, Y. Zhang, L. Guo, Novel visible light induced Co3O4-g-C3N4 heterojunction photocatalysts for efficient degradation of methyl orange, Appl. Catal. B 147 (2014) 546–553.
[59] J. Di, J. Xia, M. Ji, H. Li, H. Xu, H. Li, R. Chen, The synergistic role of carbon quantum dots for the improved photocatalytic performance of Bi2MoO6, Nanoscale 7 (2015) 11433–11443.
[60] K. Lv, X. Guo, X. Wu, Q. Li, W. Ho, M. Li, H. Ye, D. Du, Photocatalytic selective oxidation of phenol to produce dihydroxybenzenes in a TiO 2 /UV system: Hydroxyl radical versus hole, Appl. Catal. B 199 (2016) 405–411.
[61] X. Ding, W. Ho, J. Shang, L. Zhang, Self doping promoted photocatalytic removal of no under visible light with bi2moo6: Indispensable role of superoxide ions, Appl. Catal. B 182 (2016) 316–325.
[62] A.H. Mamaghani, F. Haghighat, C.-S. Lee, Photocatalytic oxidation technology for indoor environment air purification: the state-of-the-art, Appl. Catal. B 203 (2017) 247–269.
[63] S.W. Verbruggen, K. Masschaele, E. Moortgat, T.E. Korany, B. Hauchecorne, J.A. Martens, S. Lenaerts, Factors driving the activity of commercial titanium dioxide powders towards gas phase photocatalytic oxidation of acetaldehyde, Catal. Sci. Technol. 2 (2012) 2311.
[64] X. Ye, D. Chen, J. Gossage, K. Li, Photocatalytic oxidation of aldehydes: Byproduct identification and reaction pathway, J. Photochem. Photobiol. A 183 (2006) 35–40.